RESEARCH ARTICLE | MARCH 13 2025

Parametric analysis of electron beam–wave interaction in linear beam devices: A tutorial on gap coupling factor and scaling to high frequency

Md Wahidur Rahman ; Peng Zhang

AIP Advances 15, 035128 (2025)
https://doi.org/10.1063/5.0254067

Parametric analysis of electron beam–wave interaction in linear beam devices: A tutorial on gap coupling factor and scaling to high frequency

Cite as: AIP Advances 15, 035128 (2025); doi: 10.1063/5.0254067
Submitted: 20 December 2024 • Accepted: 14 February 2025 •
Published Online: 13 March 2025

Md Wahidur Rahman[1] and Peng Zhang[1,2,a)]

AFFILIATIONS

[1] Department of Electrical and Computer Engineering, Michigan State University, East Lansing, Michigan 48824, USA
[2] Department of Nuclear Engineering and Radiological Sciences, University of Michigan, Ann Arbor, Michigan 48109, USA

[a)] Author to whom correspondence should be addressed: umpeng@umich.edu

ABSTRACT

Electron beam–wave interaction is essential for particle acceleration, radiation generation, microwave and millimeter-wave communications, and fusion research. In this work, we first provide a tutorial review on the gap coupling factor, the key parameter to characterize beam cavity–gap interaction in linear beam devices, by using Carter's simple model and the disk model. We then conduct a parametric analysis of the gap coupling factor considering large signals. The gap coupling factor is investigated for different beam and tunnel radius, gap length, RF current, and anode voltage, aiming to provide guidance for the design of higher frequency devices. The effects of space charge in a large signal interaction are particularly examined, as the space charge force is responsible for energy loss and instabilities. The electron velocity change through the beam interaction gap is studied under different cavity parameters. The analysis is exemplified in a high-efficiency RF power amplifier based on an inductive output tube. The results are compared favorably against experiments and particle-in-cell simulations. We demonstrate the design of device parameters for scaling up in high frequency operations.

I. INTRODUCTION

In recent years, there has been a high demand for compact, high-power, high-frequency electromagnetic radiation sources for energy transfer, particle acceleration, beam quality control, and communications.[1–5] To meet this demand, it is crucial to increase the power of traditional vacuum electronic amplifiers, particularly in high frequency operation. Among the most promising devices are those with longitudinal interaction, such as traveling wave tubes (TWTs), klystrons, and inductive output tubes (IOTs).[6–9] Due to the reduced size of the tube's cross section in the millimeter range or even higher frequency, electron beams with high current density are required to increase the device's power.[10,11]

Perhaps, the simplest beam–circuit interaction for radiation extraction is that of a linear electron beam with a single gap cavity, as in the case of IOT. To achieve high power at high frequencies, it is necessary to use high-velocity electrons and have a small gap between the grid and the anode to avoid transit time effects.[7,12,13] However, the capacitance of the grid based operation always limits the modulation frequency and thus the operation frequency, which remains the case even for devices based on field emission arrays (FEAs).[14] Recent concept to achieve direct density modulation from the cathodes using optical means further eliminates the frequency constraints put by the RC constant of the circuit,[15] thus enabling the development of power amplifiers for wideband applications at ultra-high frequencies. A better understanding of beam–wave interaction, especially in the nonlinear, large signal regime, as well as its parametric scalings, is crucial for the design optimization of such devices.

The motivation of this work is twofold. First, we provide a simple tutorial review on determining the gap coupling factor that is used to characterize beam–wave interaction. Both the simple analytical model and the disk model will be reviewed to describe beam transport with space charge effects. Next, we conduct a

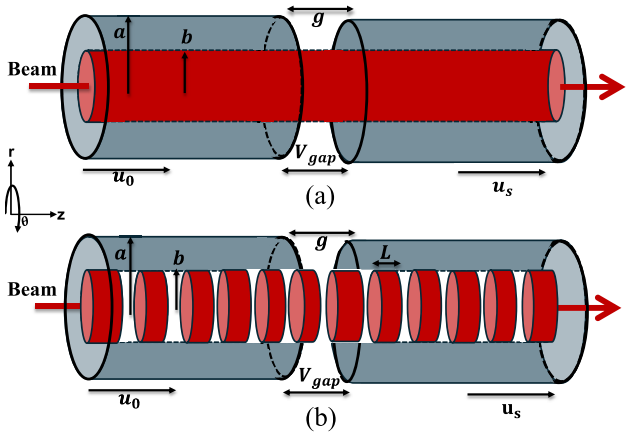

FIG. 1. Interaction gap of a linear beam device represented in (a) the simple model and (b) the disk model.

parametric analysis of beam cavity–gap interaction, considering large signals, using the analytical model and the disk model. The results are verified against experiments and particle-in-cell (PIC) simulations. The analysis is meant to set a stage for the parameter design of devices scaled up for high frequency operations, as exemplified near the end of this article.

A simple model is shown in Fig. 1(a), where an electron beam is injected along the axial z direction. The tunnel and beam radius are a and b, respectively, g is the output gap length, V_{gap} is the gap voltage, and u_0 and u_s are the initial and final velocities of electrons, respectively. In Fig. 1(b), cylindrical disks with thickness L are used to represent the beam to investigate the nonlinear space charge effects. As the beam passes through the cavity, it interacts with its electromagnetic fields, which causes the transfer of kinetic energy from the beam particles to the cavity modes, ultimately generating electromagnetic waves. To optimize this interaction, parameters such as tunnel radius, beam radius, and gap length play a crucial role. The tunnel radius affects the efficient beam confinement and optimal interaction with RF fields, the beam radius influences interaction dynamics, and the gap designs ensure efficient coupling between the beam and cavity, maximizing energy transfer.[16,17] By optimizing these parameters, it is possible to enhance device performance based on existing designs and facilitate advancements across various scientific and technological domains.

In Sec. II, we describe the models used for large signal analysis. While one can refer to textbooks and the previous literature,[18–20] for completeness and easy referencing, we also include derivations of key parameters in the Appendixes. In Sec. III, we present and discuss the results. In Sec. IV, we exemplify the device analysis for an IOT with a scale up to high frequency. A comparison with PIC simulations and experiments is also provided. Finally, we conclude our findings in Sec. V.

II. GAP COUPLING FACTOR

A. Simple model

Assume the electric field across the gap along the z direction $E(z,t) = E(z)e^{j\omega t}$, where ω is the RF frequency.[18] A general expression of the gap coupling factor is the ratio of the effective voltage, $V_{eff} = \int_o^g E(z)e^{j\beta_e z}dz$, to the RF gap voltage, $V_{gap} = \int_0^g E(z)dz$, where $\beta_e = \beta_e(u) = \omega/u$ is the beam propagation factor with u being the electron velocity.

For small signal analysis, the gap coupling factor is $M(u) = \frac{V_{eff}}{V_{gap}} = \frac{2}{\beta(u)b}\frac{I_1(\beta(u)b)}{I_0(\beta(u)a)}\frac{\sin\left(\frac{\beta(u)g}{2}\right)}{\frac{\beta(u)g}{2}}$ (see Appendix A), where I_0 and I_1 are the zeroth order and first order modified Bessel functions of the first kind, respectively. For small signal analysis, the electron velocity is assumed to be approximately a constant through the gap, and the wavenumber can be taken as a constant as $\beta(u_0) = \frac{\omega}{u_0}$. However, for large signal analysis, as the electron velocity is not constant through the gap, the initial and final wavenumbers are $\beta(u_0) = \frac{\omega}{u_0}$ and $\beta(u_s) = \frac{\omega}{u_s}$, with u_0 and u_s being the initial and final velocities of the electron, respectively. To still utilize the above expression for the gap coupling factor $M(u)$, following Carter,[20] we use $u = \frac{u_s+u_0}{2}$ for large signal analysis, which leads to

$$M_{eff} = \frac{2}{\beta\left(\frac{u_0+u_s}{2}\right)b}\frac{I_1\left(\beta\left(\frac{u_0+u_s}{2}\right)b\right)}{I_0\left(\beta\left(\frac{u_0+u_s}{2}\right)a\right)}\frac{\sin\left(\frac{\beta\left(\frac{u_0+u_s}{2}\right)g}{2}\right)}{\frac{\beta\left(\frac{u_0+u_s}{2}\right)g}{2}}. \quad (1)$$

The initial velocity is obtained from the kinetic energy of a relativistic electron, which is $eV_a = mc^2 - m_0c^2$, where V_a is the applied anode voltage, m_0c^2 is the rest energy of an electron, $m = m_0/\sqrt{1-u_0^2/c^2}$ is the relativistic mass, and c is the velocity of light. Therefore, $u_0 = c\sqrt{1-1/\left(1+\eta V_a/c^2\right)^2}$, where $\eta = e/m_0$ is the charge-to-mass ratio.[18] The final velocity, u_s, is also derived from the kinetic energy $eV_s = mc^2 - m_0c^2$, where $V_s = V_a - M_{eff}^2 I_{RF}R_L$ is the spent beam voltage, I_{RF} is the injected beam RF current, R_L is the external load impedance, and the relativistic mass is $m = m_0/\sqrt{1-u_s^2/c^2}$.[18,20] Therefore, the final velocity is

$$u_s = c\sqrt{1-1/\left(1+\frac{\eta(V_a - M_{eff}^2 I_{RF}R_L)}{c^2}\right)^2}. \quad (2)$$

We calculate M_{eff} and u_s from Eqs. (1) and (2) iteratively.

We express the gap coupling factor in normalized form as

$$M_{eff} = \frac{2}{\bar{b}}\frac{I_1\left(\bar{b}\right)}{I_0(\bar{a})}\frac{\sin\left(\frac{\bar{g}}{2}\right)}{\left(\frac{\bar{g}}{2}\right)}, \quad (3)$$

where the normalized tunnel, beam radius, and gap length are $\bar{a} = \frac{a}{L}, \bar{b} = \frac{b}{L}, \bar{g} = \frac{g}{L}$, respectively, with the length scale $L = 1/\beta\left(\frac{u_0+u_s}{2}\right)$.

B. Disk model

The current bunches rapidly disperse in the z direction after exiting the electron beam–wave interaction gap due to space-charge effects and velocity spread that cause the spent beam to behave like a multi-velocity DC beam. A more precise approach involves considering the current pulses as consecutive cylinder disks of space charge [Fig. 1(b)].[21] We use Green's function to calculate the potential distribution in cylinder.[22]

The axial electric field averaged over the beam is given by (see Appendix B)[20]

$$E_z(z) = \frac{V_{gap}}{2\pi}\int_{-\infty}^{\infty}\frac{2}{\beta b}\frac{I_1(\beta b)}{I_0(\beta a)}\frac{\sin(\beta g/2)}{\beta g/2}e^{-j\beta z}d\beta. \quad (4)$$

For the disk model, we estimate the gap voltage $V_{gap} = I_{RF}M_{eff}R_L$ from the simple model in order to provide a direct comparison with the simple model.[20] In the calculation, we integrate Eq. (4) from 0 to $\frac{m\pi}{g}$ to get the value of $E_z(z)$, where g is the gap length, and we use $m = 50$ to consider a broader range of frequencies. The axial electric field due to space charge potential outside and inside of a cylindrical disk charge of radius b located from $z = -L/2 + z_i$ to $L/2 + z_i$ (with z_i being the center of the disk) inside an earthed conducting cylinder of radius a averaged over the disk cross section is (see Appendix C)[22–25]

$$E_{sc1} = \mathrm{sgn}(z - z_i)\frac{4\rho_c}{\varepsilon_0}\sum_{m=1}^{\infty}\frac{1}{\mu_m}\frac{[J_1(\mu_m b)]^2}{(\mu_m a)^2[J_1(\mu_m a)]^2} \times e^{-\mu_m|z-z_i|}\sinh\left(\frac{\mu_m L}{2}\right) \quad (5)$$

for $|z - z_i| > L/2$ and

$$E_{sc2} = \frac{4\rho_c}{\varepsilon_0}\sum_{m=1}^{\infty}\frac{1}{\mu_m}\frac{[J_1(\mu_m b)]^2}{(\mu_m a)^2[J_1(\mu_m a)]^2}e^{-\frac{\mu_m L}{2}}\sinh\mu_m(z - z_i) \quad (6)$$

for $|z - z_i| \le L/2$.

The velocity, u_s, of the charge disk can then be calculated from the equation of motion, where SC is the space charge; $SC = 1$ and $SC = 0$ are used when the space charge effect is present and absent, respectively (see Appendix D),[26]

$$\frac{du_{s_i}}{dt} = \eta\left(1 - \frac{u_0^2}{c^2}\right)^{3/2}\left[E_z(z_i)\cos(\omega t) + SC\sum_{j=1}^{N_D}\frac{Q}{e}E_{sc1,2}(z_i - z_j)\right]. \quad (7)$$

Here, the number of electrons in one disk is $\frac{Q}{e}$, where Q is the charge in the disk, $E_z(z)$ is the electric field due to the gap given in Eq. (4), and E_{sc1} and E_{sc2} are given by Eqs. (5) and (6), respectively, with setting $\rho_c = \frac{q}{\pi b^2 L} = \frac{e}{\pi b^2 L}$.

The kinetic energy of the charge disks with charge Q is found to be (see Appendix D)

$$KE_k = \frac{Q}{\eta}c^2\sum_{j=1}^{N_D}\left(1/\sqrt{1 - \frac{u_{s_{k,j}}^2}{c^2}} - 1\right), \quad (8)$$

where $k(= 1, 2, \ldots)$ is the time step.

The model operates by injecting an RF current, where I_{RF} is used to calculate the gap voltage and DC beam current I_b is used to calculate the disk charge. The calculation relies on using $N_D(=50)$ rigid disks with the same dimensions and charges to represent the beam over one RF period. The initial position of the bunch is set to be far from the gap that allows all electrons to start their motion outside the gap field. Furthermore, we set the final time to be long enough for all electrons to exit the gap field.[18,19] From Eq. (7), the E field on the disks i (for $i = 1, \ldots N_D$) at position z_i equals the sum of the axial field $E_z(z)$ at z_i and the field due to the space charge of disks at position z_j (for $j = 1, \ldots N_D$) and $j \neq i$ [i.e., the field due to its own space charge of disk i is 0, as seen from Eq. (6)]. In our calculation, the center of the gap is located at $z = 0$, the initial time is $t_0 = 0$ ns when the bunching center position is $z_0 = \frac{-4\pi}{\beta(u_0)} = -0.14$ m, the total time is $t_f = 3$ ns when all the disks had left the field of the gap, and the time interval $\Delta t = \frac{t_f - t_0}{100} = 0.03$ ns, where the number of time steps is 100. The initial position of the disk is $z_{initial} = z_0 + (\frac{N_D+1}{2} - i)L$,[26] where $L(=0.8$ mm) is the thickness of the disk. Therefore, the initial positions of the first and N_Dth disk are −0.12 and −0.16 m, respectively. Next, we numerically integrate Eq. (7) over a series of fixed steps (a total of 100 time steps). The result will be a table, where the first column will show the time, followed by columns showing the positions of the disks and the velocity of the electrons. Finally, we use the final velocity of electrons to calculate the kinetic energy.

We calculate the charge in each disk as $Q = \frac{I_b}{fN_D}$,[26] where $N_D(= 50)$ is the number of rigid disks, f is the frequency, and I_b is the injected DC beam current,[18,26] in order to calculate the kinetic energy by using Eq. (8).

III. PARAMETRIC ANALYSIS OF BEAM–GAP INTERACTION

Unless otherwise stated, we use the following default values in our calculations for the interaction of a beam with a single gap: $a = 11$ mm, $b = 6.5$ mm, $g = 11$ mm, $R_L = 26$ kΩ, $f = 1.3$ GHz, $I_b = 0.9$ A, $I_{RF} = 1.4$ A, and $V_a = 25$ kV. In the case of parametric analysis of the interaction on the dependence of a certain parameter, all the other parameters are kept the same as these default values.

The gap coupling factor M calculated from the simple model and the disk model with and without space charge effects is shown in Fig. 2 for different injected RF input currents I_{RF}. It is clear that the small signal analysis is independent of I_{RF} and gives the largest M. For a small I_{RF}, all the models yield similar values and the small signal analysis is a good approximation. However, as I_{RF} increases, the gap coupling factor decreases using the large signal simple model and the disk model. Including the space charge effect further reduces the value of M. The reduction in M with increasing I_{RF} can be seen from Eqs. (1) and (2). From Eq. (2), the final electron velocity u_s decreases as the RF current I_{RF} increases, which leads to an increase in the wavenumber $\beta(u) = \frac{\omega}{u_0 + u_s}$ and, consequently, a decrease in the gap coupling factor as seen from Eq. (1).

In Fig. 3, the gap coupling factor M is plotted against the tunnel radius a, beam radius b, gap length g, load resistance R_L, frequency f, and applied anode voltage V_a. When the tunnel radius and gap length of the tunnel are decreased, M increases by improving electron beam interaction with the RF field and reducing transit time spread. In practice, it is typically chosen that the gap length is nearly equal to the tunnel radius, ensuring balanced radial field uniformity and resistance to field variations within the gap, which helps prevent electrical breakdown and multipactor discharge.[18,27,28] For a larger beam radius, both the simple and disk models show a higher M due to increased field experienced by the beam and reduced space charge effects for a fixed beam current. However, to prevent the interception of electrons on the drift tube, the radius of the electron beam

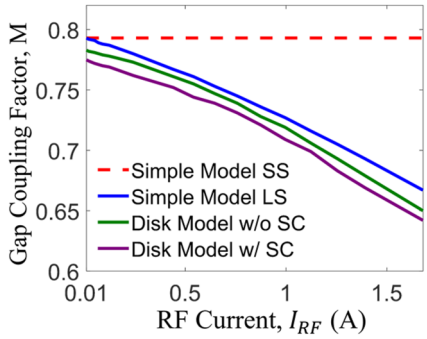

FIG. 2. Comparison of the gap coupling factor of the simple model for small signal (SS) and large signal (LS) analyses and the disk model with and without space charge (SC) as a function of different RF currents.

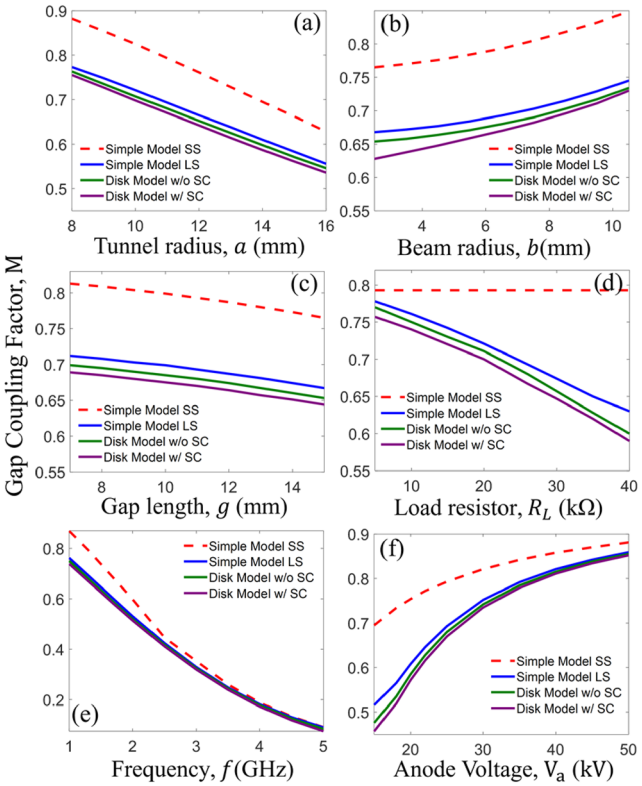

FIG. 3. Comparison of the gap coupling factor of the simple and disk models with and without space charge for different (a) tunnel radius a, (b) beam radius b, (c) gap length g, (d) load resistor R_L, (e) frequency f, and (f) anode voltage V_a.

is usually limited to $2a/3$.[18] Increased load resistor results in lowering the gap coupling factor, where the dependence of M on R_L is similar to that on I_{RF} as shown in Fig. 2. Increasing the frequency implies increasing the wavenumber in order to maintain the synchronization between the beam and the wave as $\beta_e z \cong \omega t$, which leads to a reduction in M [cf. Eq. (1)]. For an IOT, the operation frequency of the grid is capped at ~1.3 GHz.[20,29] However, with optical gating for beam density modulation during emission,[15] a much higher frequency can be achieved, where parametric scaling analysis to increase the gap coupling factor is important. A higher anode voltage, V_a, leads to a higher beam energy and electron velocity, which reduces the wavenumber β and thus increases M. For all the cases presented, in the presence of negative space charge effect in the output gap, the gap coupling factors are always lower compared to that from the simple model and the disk model without space charge. In the cases presented, including space charge effects in the disk model show a reduction of up to 3.85% in the gap coupling factor.

In Fig. 4, the gap coupling factor M is shown in terms of normalized tunnel radius $\bar{a}$, beam radius $\bar{b}$, and gap distance $\bar{g}$ in Eq. (3), which is valid for the simple model for both the small signal and large signal analysis. We can see that the increase in normalized tunnel radius $\bar{a}$ and gap length $\bar{g}$ lowers the M, whereas the increase in normalized beam radius $\bar{b}$ increases the M.

Figure 5 illustrates the average electric field, $\frac{E_z(z)}{V_{gap}/g}$ [from Eq. (4)], acting on electrons in the axial direction. The changes in the tunnel radius, beam radius, and gap length impact the electric field distribution and subsequently affect the behavior of the electron beam. In particular, increasing the beam radius and lowering the tunnel radius and gap length can enhance the electric field strength in the gap that accelerates electrons, which is consistent with the increase in the gap coupling factor, as shown in Figs. 3 and 4.

Figure 6 shows the normalized velocities (in terms of the initial velocity) when electrons pass through the gap calculated from the disk model with and without space charge effects. The vertical dashed lines represent the physical edges of the gap in the beam tunnel. Decreasing the tunnel radius, increasing the beam radius, and decreasing the gap length all result in lowering the final velocity of electrons and thus a higher energy transfer from the beam to

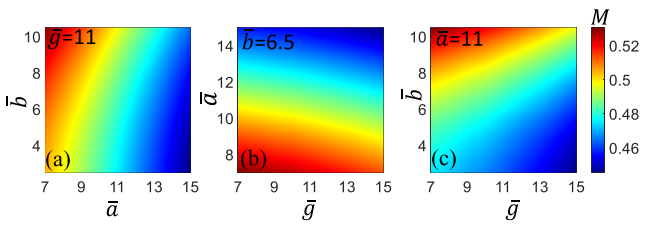

FIG. 4. Comparison of the gap coupling factor as a function of normalized (a) $\bar{a}$ and $\bar{b}$ for fixed $\bar{g}$ = 11, (b) $\bar{g}$ and $\bar{a}$ for fixed $\bar{b}$ = 6.5, and (c) $\bar{g}$ and $\bar{b}$ for fixed $\bar{a}$ = 11.

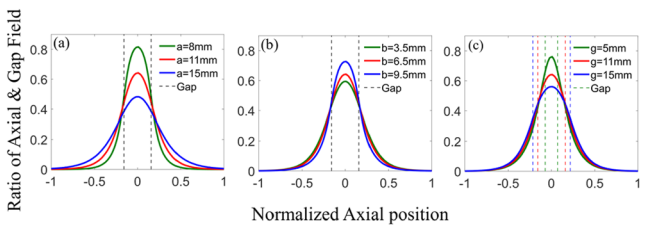

FIG. 5. Variation of axial electric field of the disk model for different values of (a) tunnel radius a, (b) beam radius b, and (c) gap length g.

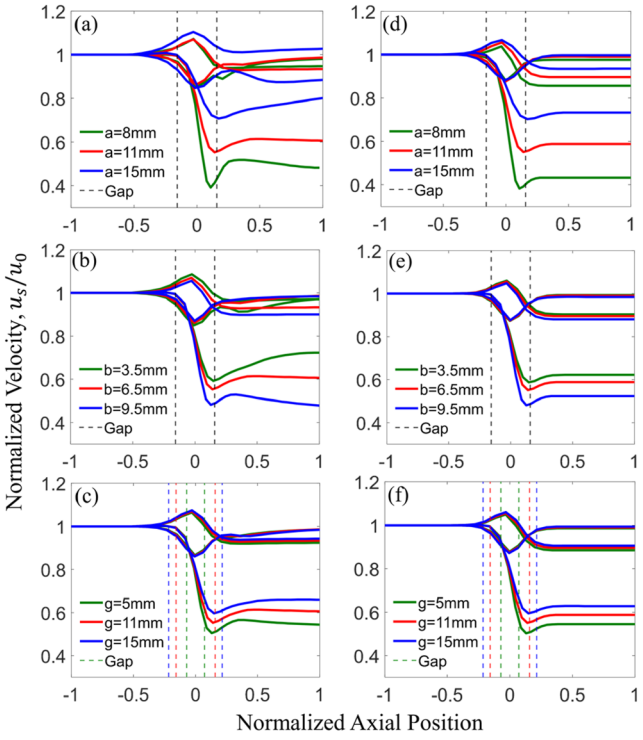

FIG. 6. Normalized electron velocity of the disk model with [(a)–(c)] and without [(d)–(f)] space charge for different values of [(a), (d)] tunnel radius, [(b), (e)] beam radius, and [(c), (f)] gap length.

microwave, which is consistent with the parametric dependence of the gap coupling factor shown in Figs. 2–4. Furthermore, the final velocity of the electrons at the exit of the gap is higher and the velocity spread is larger for the presence of space charge, which increases the beam kinetic energy and decreases the RF efficiency.

Figure 7 shows that the normalized kinetic energy, $\frac{\sum KE/N_D}{KE_0}$, is decreased when there is a decrease in tunnel radius and gap length, or an increase in beam radius, where the total kinetic energy is summed over all the N_D disks and KE_0 is the initial kinetic energy of one disk. The reduction in the kinetic energy means that more efficient power transfer from the electron beam, which again is consistent with the gap coupling factor characterization above.

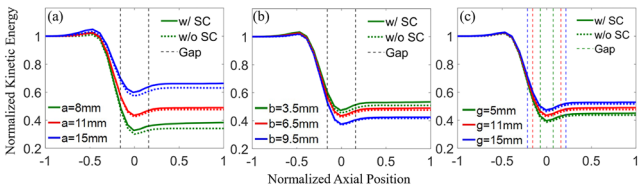

FIG. 7. Normalized kinetic energy of the disk model with (solid lines) and without (dotted lines) space charge for different values of (a) tunnel radius, (b) beam radius, and (c) gap length.

Including space charge in the gap results in a higher electron velocity, resulting in an increase in kinetic energy and a reduction in efficiency.[30]

IV. AN IOT EXAMPLE WITH SCALE UP TO HIGH FREQUENCY

IOT is operated as a common grid amplifier. The DC and first harmonic of the RF beam current can be determined using the Fourier analysis of the emission beam current. The RF output power is dependent on the injected RF current, gap coupling factor, and load impedance, R_L,

$$P_{out} = \frac{1}{2} M_{eff}^2 I_{RF}^2 R_L. \tag{9}$$

The efficiency of the IOT is

$$\eta_e = \frac{P_{out}}{I_b V_a}, \tag{10}$$

where I_b(=0.9 A) is the DC beam current[18,20] and V_a is the anode voltage.

The RF power and efficiency of IOT at 1.3 GHz calculated from the large signal simple model and disk model are shown in Fig. 8. Both the RF output power and efficiency increase when the tunnel radius or gap length decreases, as it enhances interaction with the RF field and reduces the electron transit time, respectively.[16,17,27] For a larger beam radius, the output power and efficiency are higher as there is better coupling between the beam and the gap with less space charge effect for a fixed beam current.[16,22] As the load resistor R_L increases, although the gap coupling factor decreases [Fig. 3(d)], both the RF output power and the efficiency increase as $P_{out} \propto R_L$ [see Eq. (9)]. When the frequency is increased, the time for electron interaction with the RF fields decreases as the RF cycles happen more quickly. Fewer electrons may effectively contribute to RF power generation, resulting in reduced output power and energy transfer efficiency. When the anode voltage increases, the output power of the amplifier increases because of the increase in the gap coupling factor [Fig. 3(f)]; however, the efficiency decreases as $\eta_e \propto \frac{1}{V_a}$ [see Eq. (10)].

Figure 8 also shows that our calculations using the simple model agree well with the experimental results extracted using the simple model in Refs. 20 and 31; and calculations using the disk model with space charge effects have a reasonable agreement with the PIC simulation results, with the same parameters as the default values listed at the beginning of Sec. III. In the PIC simulations, a single cavity gap was set up in XOOPIC,[32] where an external axial magnetic field of 0.6 T was applied to reduce the expansion of the electron beam. Using the default parameters, the RF output power and efficiency are 10.79 kW and 47.9% for the PIC simulation, while our disk model with space charge shows 11.29 kW and 50.8%, respectively. As seen from Fig. 8, in general, the large signal simple model overestimates the RF power and efficiency. While the simple model can provide a quick estimation of the scaling, more accurate calculations require the use of the disk model with

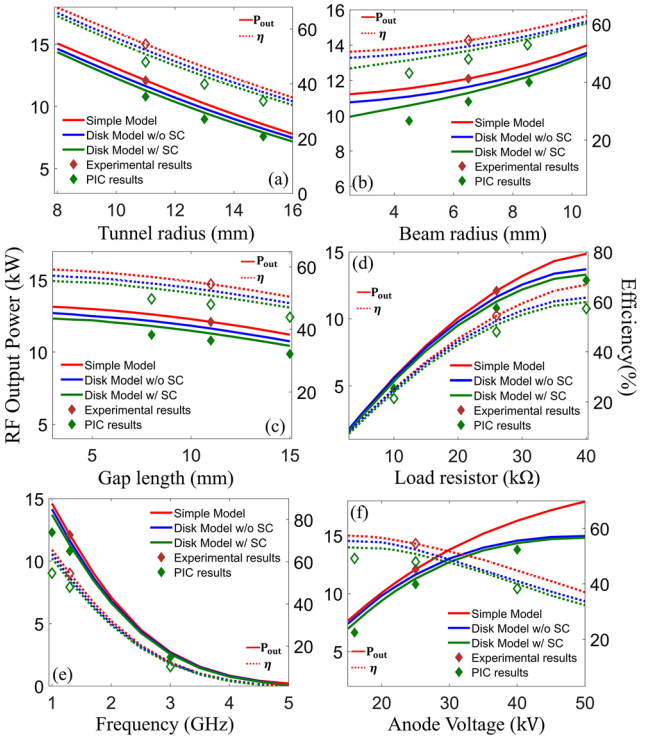

FIG. 8. Comparison of RF output power (solid lines) and efficiency (dotted lines) from the large signal simple model and disk model with and without space charge (SC) for different values of (a) tunnel radius a, (b) beam radius b, (c) gap length g, (d) load resistor R_L, (e) frequency f, and (f) anode voltage V_a. The symbols are for experimental results obtained using the simple model in Refs. 20 and 31 and for PIC results using XOOPIC.

space charge effects or PIC simulations if the computational cost is affordable.

At higher frequencies, the RF output power and efficiency drop significantly [see Fig. 8(e)]. It is thus important to find out how to enhance both the output power and efficiency at high frequencies by tuning the device parameters based on existing design. In this example, we assume that the same cathode is used as in the 1.3 GHz frequency case as in Fig. 8, where the beam radius b is kept at 6.5 mm. In Fig. 9(a), we observe that reducing the tunnel radius a improves both the output power and efficiency at 5 GHz, with all other parameters as the default values listed at the beginning of Sec. III. By adopting $a = 7.5$ mm with all the other parameters as default values, Fig. 9(b) shows that decreasing g further increases P_{out} and η_e. In Fig. 9(c), with fixed $a = 7.5$ mm and $g = 3$ mm, it shows that a higher R_L leads to an increase in P_{out} and η_e. Finally, Fig. 9(d) demonstrates that the device's efficiency can be further enhanced by increasing the injected RF current, which can be realized by electron emission with a higher modulation depth, e.g., using optical means.[15] By using $a = 7.5$ mm, $g = 3$ mm, $R_L = 50$ kΩ, and $I_{RF} = 1.9$ A at $f = 5$ GHz, the RF output powers are 13.62, 11.49, and 12.48 kW, with efficiencies of 45.4%, 38.3%, and 41.6% for the simple and disk models with and without space charge, respectively.

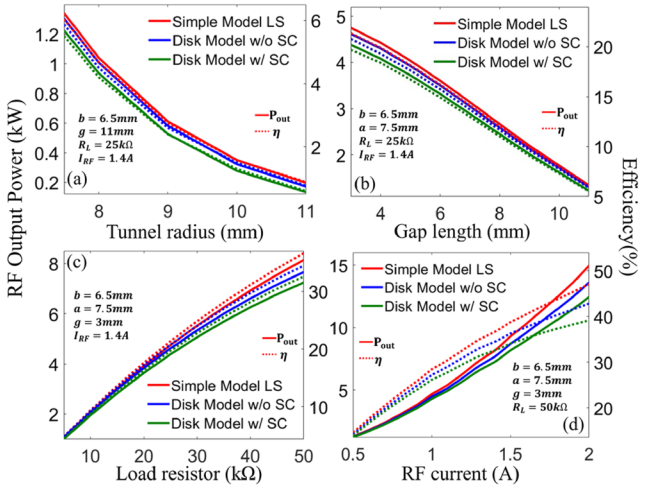

FIG. 9. RF output power (solid lines) and efficiency (dotted lines) from the simple model and disk model with and without space charge (SC) at 5 GHz for different values of (a) tunnel radius a, (b) gap length g, (c) load resistor R_L, and (d) RF current I_{RF}.

V. CONCLUSION

In this study, we provide a brief tutorial of the gap coupling factor using the simple and disk models for extracting energy from electron beams and generating RF power. We considered the effects of space charge in the disk model and provided a parametric analysis of the gap coupling factor for its dependence on beam and tunnel radius, gap length, frequency, and beam energy. It is found that the RF output power and efficiency are lowered due to the presence of space charge (see Fig. 8), which is attributed to the increased kinetic energy of the electron beam after interaction due to the distortion of electron trajectories by the space charge force. Increasing the beam filling factor (i.e., increasing beam radius or decreasing tunneling radius) and decreasing the gap length lower the kinetic energy (see Fig. 7) and enhance conversion efficiency, which can aid in the design of beam interaction circuit, as exemplified in an IOT amplifier with a scale up to high frequency operation. While the simple model can be useful to quickly predict the parametric scaling, it overestimates the gap coupling factor as compared to the disk models. The results from the disk models with space charge are compared favorably with PIC simulations. Disk models with the space charge effect may be used to more accurately estimate the RF power and efficiency than the simple model, and with less computational cost than PIC simulations.

Future studies may include the study of gap coupling factor for different beam profiles (both transverse and longitudinal) and its connection with electron bunching mechanisms in beam–gap interactions.[33–35]

ACKNOWLEDGMENTS

This work was supported by the Office of Naval Research (ONR) YIP under Grant No. N00014-20-1-2681, the Air Force

Office of Scientific Research (AFOSR) under Grant No. FA9550-20-1-0409, and the Air Force Office of Scientific Research (AFOSR) under Grant No. FA9550-22-1-0523.

AUTHOR DECLARATIONS

Conflict of Interest

The authors have no conflicts to disclose.

Author Contributions

Md Wahidur Rahman: Data curation (equal); Formal analysis (equal); Investigation (equal); Methodology (equal); Validation (equal); Visualization (equal); Writing – original draft (equal). **Peng Zhang**: Conceptualization (equal); Formal analysis (equal); Funding acquisition (equal); Investigation (equal); Methodology (equal); Project administration (equal); Supervision (equal); Validation (equal); Visualization (equal); Writing – review & editing (equal).

DATA AVAILABILITY

The data that support the findings of this study are available within the article.

APPENDIX A: SIMPLE MODEL SIGNAL GAP COUPLING FACTOR

For a gap electric field, $E(z,t) = E(z)e^{j\omega t}$, and the RF gap voltage is $V_{gap} = \int_0^g E(z)dz$. The acceleration of the electron within the gap field is given by the equation of motion,[36]

$$\frac{d^2z}{dt^2} = \frac{e}{m}E(z)e^{j\omega t}, \tag{A1}$$

where e and m are the electron charge and mass, respectively. Multiplying both sides of Eq. (A1) by $2dz$, we obtain the derivative of the square of velocity, $2\frac{dz}{dt}\frac{d^2z}{dt^2}dt = \frac{d}{dt}\left(\frac{dz}{dt}\right)^2 dt = 2\frac{e}{m}E(z)e^{j\omega t}dz$. After integration in terms of z from 0 to z, with initial electron velocity u_0, we get

$$\left(\frac{dz}{dt}\right)^2 - u_o^2 = 2\frac{e}{m}\int_0^z E(z)e^{j\omega t}dz. \tag{A2}$$

Assuming a small RF modulation (i.e., small signal approximation), we have $\beta_e z \cong \omega t$. Substituting this into Eq. (A2) and integrating from $z = 0$ (when $t = 0$) to the end of the gap, we get $\frac{1}{2}m\left[u^2 - u_0^2\right] = e\int_0^g E(z)e^{j\beta_e z}dz$, where u is the exit velocity of the electron, and the energy change of the electron due to its interaction with the gap $\frac{1}{2}m\left[u^2 - u_0^2\right] = eMV_{gap} = eV_{eff}$.[36] Therefore, $V_{eff} = \int_0^g E(z)e^{j\beta_e z}dz$ and the gap coupling factor becomes $M = \frac{V_{eff}}{V_{gap}} = \frac{\int_0^g E(z)e^{j\beta_e z}dz}{\int_0^g E(z)dz}$. This expression may be generalized by extending the integration over the entire z axis (e.g., for a gridless gap or a gap with considerable field outside the physical opening) to yield $M(\beta_e) = \frac{\int_{-\infty}^{\infty} E(z)e^{j\beta_e z}dz}{\int_{-\infty}^{\infty} E(z)dz}$.

For a constant electric field $E(z) = \frac{V_{gap}}{g}$ across the gap from $-g/2$ to $g/2$, taking the real part of the integral, we have

$$M(\beta_e) = \frac{\frac{V_{gap}}{g}\int_{-g/2}^{g/2}\cos(\beta_e z)dz}{V_{gap}} = \frac{\sin\left(\frac{\beta_e g}{2}\right)}{\frac{\beta_e g}{2}}. \tag{A3}$$

For the cylindrical geometry in Fig. 1(a), the field can be solved from Maxwell's equations in the absence of space charge (i.e., the wave equation), which yields the approximate solution $E_z(r,z,t) = f(z)I_0(\gamma r)e^{j\omega t} \propto I_0(\gamma r)e^{j\beta z}e^{j\omega t}$, with $\gamma^2 = \beta^2 - k^2$ (>0), $k = \omega/c$, and β being the axial wavenumber, which is assumed to be close to the beam propagation factor β_e.[36]

The electric field averaged over the beam's cross section area $A = \pi b^2$ thus becomes $E_z(z,t) = \frac{1}{A}\int_0^b 2\pi r I_0(\gamma r)f(z)e^{j\omega t}dr = \frac{2\pi}{A}f(z)e^{j\omega t}\int_0^b rI_0(\gamma r)dr = 2f(z)e^{j\omega t}\frac{I_1(\gamma b)}{\gamma b}$. Again, assuming small signal and using $\beta_e z \cong \omega t$ during electron's transit across the gap from $-g/2$ to $g/2$, the effective voltage becomes $V_{eff} = \int_{-g/2}^{g/2} E_z(z)e^{j\beta_e z}dz = \int_{-g/2}^{g/2} 2f(z)\frac{I_1(\gamma b)}{\gamma b}e^{j\beta_e z}dz = 4\frac{I_1(\gamma b)}{\gamma b}\frac{f_0}{\beta_e}\sin\left(\frac{\beta_e g}{2}\right)$, where we have taken only the real part of the integral and assumed no variation of the field along the z direction inside the gap, i.e., $f(z) = f_0$ [cf. Eq. (A3)]. The gap voltage at $r = a$ is $V_{gap}(r=a) = \int_{-g/2}^{g/2} E(r=a,z)dz = \int_{-g/2}^{g/2} f(z)I_0(\gamma a)dz = gf_0I_0(\gamma a)$. Assuming that the wavenumber is close to the beam propagation constant and since $u \ll c$, we have $\gamma^2 \cong \gamma_e^2 = \beta_e^2 - k^2 = (\omega/u)^2 - (\omega/c)^2 \cong (\omega/u)^2 = \beta_e^2$. Thus, we can approximate $V_{eff} \cong 4\frac{I_1(\beta_e b)}{\beta_e b}\frac{f_0}{\beta_e}\sin\left(\frac{\beta_e g}{2}\right)$ and $V_{gap}(r=a) = gf_0I_0(\gamma a) \cong gf_0I_0(\beta_e a)$.

For small signal analysis, where V_{gap} is small and the electron velocity remains nearly constant, the gap coupling coefficient is

$$M(\beta(u)) = \frac{V_{eff}}{V_{gap}(r=a)} = \frac{2}{\beta_e(u)b}\frac{I_1(\beta_e(u)b)}{I_0(\beta_e(u)a)}\frac{\sin\left(\frac{\beta_e(u)g}{2}\right)}{\frac{\beta_e(u)g}{2}}. \tag{A4}$$

For large signal analysis, the electron velocity exiting the gap u_s is different from the entering velocity u_0, so $u = \frac{u_s+u_0}{2}$ is used in calculating the gap coupling coefficient,

$$M\left(\beta\left(\frac{u_0+u_s}{2}\right)\right) = \frac{2}{\beta\left(\frac{u_0+u_s}{2}\right)b}\frac{I_1\left(\beta\left(\frac{u_0+u_s}{2}\right)b\right)}{I_0\left(\beta\left(\frac{u_0+u_s}{2}\right)a\right)}\frac{\sin\left(\frac{\beta\left(\frac{u_0+u_s}{2}\right)g}{2}\right)}{\frac{\beta\left(\frac{u_0+u_s}{2}\right)g}{2}}. \tag{A5}$$

APPENDIX B: GAP FIELD

For a piecewise-continuous electric field across the gap $E_z(z)$, it can be written in terms of the inverse Fourier integral,

$$G(\beta) = \frac{1}{2\pi}\int_{-\infty}^{\infty} E_z(z)e^{j\beta z}dz, \tag{B1}$$

which is in the same form as the numerator of the gap coupling factor [see the last expression in the end of the paragraph before Eq. (A3)]. This means that M can be written in terms of the Fourier transform of the electric field,

$$M(\beta) = \frac{\int_{-\infty}^{\infty} E(z)e^{j\beta z}dz}{\int_{-\infty}^{\infty} E(z)dz} = \frac{2\pi}{V_{gap}}G(\beta). \tag{B2}$$

Comparing Eqs. (A4) and (B2) yields an effective inverse Fourier integral for the axial electric field averaged over the beam,

$$G_{eff}(\beta) = \frac{V_{gap}}{2\pi} M(\beta) = \frac{V_{gap}}{2\pi} \frac{2}{\beta b} \frac{I_1(\beta b)}{I_0(\beta a)} \frac{\sin(\beta g/2)}{\beta g/2}, \tag{B3}$$

based on which the axial component of the electric field averaged over the beam can be obtained as $E_z(z) = \int_{-\infty}^{\infty} G_{eff}(\beta) e^{-j\beta z} d\beta$, leading to

$$E_z(z) = \frac{V_{gap}}{2\pi} \int_{-\infty}^{\infty} \frac{2}{\beta b} \frac{I_1(\beta b)}{I_0(\beta a)} \frac{\sin(\beta g/2)}{\beta g/2} e^{-j\beta z} d\beta, \tag{B4}$$

which is the same as Eq. (6) of Carter.[20]

APPENDIX C: SPACE CHARGE FIELD

Using Green's function, we calculate the potential voltage when a charge q is placed at the point $z = 0, r = r_0, \phi = \phi_0$, inside an earthed conducting cylinder of radius a shown in p. 188 of Ref. 37. The potential of the point charge for positive z is

$$V_{point} = \sum_{m=1}^{\infty} \sum_{n=0}^{\infty} A_{mn} e^{-\mu_m z} J_n(\mu_m r) \cos n(\phi - \phi_0), \tag{C1}$$

where J_n is the nth order Bessel function of the first kind and μ_m is chosen so that $J_n(\mu_m a) = 0$. Differentiating Eq. (C1) and setting $z = 0$ give $\frac{dV}{dz}\big|_0 = -\sum_{m=1}^{\infty} \sum_{n=0}^{\infty} \mu_m A_{mn} J_n(\mu_m r) \cos n(\phi - \phi_0)$, which, due to symmetry, is zero except at the point charge itself. After multiplying $rJ_p(\mu_s r)\cos p(\phi - \phi_0)$ on both sides and integrating from $r = 0$ to $r = a$ and from $\phi = 0$ to $\phi = 2\pi$, all terms on the right disappear unless $p = n$ and $s = m$, which leads to

$$A_{mn} = \frac{-\int_0^a dr \int_0^{2\pi} d\phi \frac{dV}{dz}\big|_0 r J_n(\mu_m r) \cos n(\phi - \phi_0)}{\int_0^a dr \int_0^{2\pi} d\phi r \mu_m [J_n(\mu_m r)]^2 [\cos n(\phi - \phi_0)]^2}. \tag{C2}$$

We can evaluate the lower part of Eq. (C2), where $\int_0^a r\mu_m [J_n(\mu_m r)]^2 dr = \frac{1}{2} a^2 \mu_m \{[J_n(\mu_m a)]^2 + [J_{n+1}(\mu_m a)]^2\} - naJ_n(\mu_m a) J_{n+1}(\mu_m a) = \frac{1}{2} a^2 \mu_m [J_{n+1}(\mu_m a)]^2$, and the ϕ integration gives a factor of π if $n > 0$ and 2π if $n = 0$. Thus, Eq. (C2) becomes

$$A_{mn} = \frac{-(2 - \delta_n^0)}{\pi \mu_m [a J_{n+1}(\mu_m a)]^2} \int_0^a dr \int_0^{2\pi} d\phi \frac{dV}{dz}\bigg|_0 r J_n(\mu_m r) \cos n(\phi - \phi_0), \tag{C3}$$

where $\delta_n^0 = 1$ when $n = 0$ and $\delta_n^0 = 0$ as $n \neq 0$.[22,37]

In the $z = 0$ plane, for a point charge, the area $\triangle s$ in which $\frac{dV}{dz}\big|_0 \neq 0$ is taken so small that in it $J_n(\mu_m r)$ has the constant value $J_n(\mu_m r_0)$ and $\cos n(\phi - \phi_0) = 1$. The integral in Eq. (C3) then becomes $J_n(\mu_m r_0) \int_0^a \int_0^{2\pi} \frac{dV}{dz}\big|_0 r dr d\phi = J_n(\mu_m r_0) \int_{\triangle s} \frac{dV}{dn} ds = -\frac{q}{2\varepsilon_0} J_n(\mu_m r_0)$, where we have used Gauss's electric flux theorem, remembering that only half the flux passes one side of the area. From Eq. (C3), we get $A_{mn} = \frac{(2-\delta_n^0) q J_n(\mu_m r_0)}{2\pi\varepsilon_0 \mu_m a^2 [J_{n+1}(\mu_m a)]^2}$, which can be inserted into Eq. (C1) to get the potential voltage of a point charge q inside a conducting cylinder.

We next calculate the potential voltage of a ring of charge placed at $z = 0, r = r_0$, with the uniform line charge density of $\rho_r = \frac{q}{2\pi r_0}$, inside an earthed conducting cylinder of radius a, which can be obtained by integrating Eq. (C1) in terms of ϕ_0 from 0 to 2π to give

$$V_{ring} = \sum_{m=1}^{\infty} \frac{\rho_r J_0(\mu_m r_0)}{\varepsilon_0 \mu_m a^2 [J_1(\mu_m a)]^2} e^{-\mu_m |z|} J_0(\mu_m r). \tag{C4}$$

The potential of the circular area of space charge extending from $r = 0$ to $r = b$ placed at $z = 0$, with the uniform surface charge density of $\rho_d = \frac{q}{\pi b^2}$, inside an earthed conducting cylinder of radius a, can then be obtained by integrating Eq. (C4) in terms of r_0 from 0 to b, to obtain

$$\begin{aligned} V_{circular\ area} &= \sum_{m=1}^{\infty} \frac{\rho_d J_0(\mu_m r)}{\varepsilon_0 \mu_m a^2 [J_1(\mu_m a)]^2} e^{-\mu_m |z|} \int_0^b r_0 J_0(\mu_m r_0) dr_0 \\ &= \sum_{m=1}^{\infty} \frac{\rho_d b J_1(\mu_m b)}{\varepsilon_0 \mu_m^2 a^2 [J_1(\mu_m a)]^2} J_0(\mu_m r) e^{-\mu_m |z|}. \end{aligned} \tag{C5}$$

Next, we consider a cylindrical disk of uniform charge density $\rho_c = \frac{q}{\pi b^2 L}$ from $z_0 = -L/2$ to $L/2$ and with radius of b, inside an earthed conducting cylinder of radius a. By integrating Eq. (C5) over z_0, we can obtain the outside potential of a cylinder of space charge where $|z| > \frac{L}{2}$ and the inside potential where $|z| < \frac{L}{2}$.[22]

For potential outside of the cylindrical disk charge,

$$V_1 = \sum_{m=1}^{\infty} \int_{-L/2}^{L/2} \frac{\rho_c b J_0(\mu_m r) J_1(\mu_m b)}{\varepsilon_0 \mu_m^2 a^2 [J_1(\mu_m a)]^2} e^{-\mu_m |z - z_0|} dz_0, \tag{C6}$$

where $z > \frac{L}{2} \geq z_0$ for positive z, so we use $|z - z_0| = z - z_0$, as shown in Fig. 10(a). Thus, Eq. (C6) gives $V_1 = \sum_{m=1}^{\infty} \frac{2\rho_c b J_0(\mu_m r) J_1(\mu_m b)}{\varepsilon_0 \mu_m^2 a^2 [J_1(\mu_m a)]^2} e^{-\mu_m z} \left(\frac{1}{\mu_m}\right) \sinh\left(\frac{\mu_m L}{2}\right)$.

For potential inside of the cylindrical disk charge,

$$\begin{aligned} V_2 = \sum_{m=1}^{\infty} &\int_{-\frac{L}{2}}^{z} \frac{\rho_c b J_0(\mu_m r) J_1(\mu_m b)}{\varepsilon_0 \mu_m^2 a^2 [J_1(\mu_m a)]^2} e^{-\mu_m (z - z_0)} dz_0 \\ &+ \int_{z}^{L/2} \frac{\rho_c b J_0(\mu_m r) J_1(\mu_m b)}{\varepsilon_0 \mu_m^2 a^2 [J_1(\mu_m a)]^2} e^{-\mu_m (z_0 - z)} dz_0, \end{aligned} \tag{C7}$$

where we consider two conditions as $z > z_0$, so $|z - z_0| = z - z_0$, and $z < z_0$, so $|z - z_0| = z_0 - z$ as shown in Figs. 10(b) and 10(c). Therefore,

$$V_2 = \sum_{m=1}^{\infty} \frac{\rho_c b J_0(\mu_m r) J_1(\mu_m b)}{\varepsilon_0 \mu_m^2 a^2 [J_1(\mu_m a)]^2} \left[e^{-\mu_m z} \int_{-\frac{L}{2}}^{z} e^{\mu_m z_0} dz_0 + e^{\mu_m z} \int_{z}^{\frac{L}{2}} e^{-\mu_m z_0} dz_0 \right]. \tag{C8}$$

The integration of Eq. (C8) gives $V_2 = \sum_{m=1}^{\infty} \frac{2\rho_c b J_0(\mu_m r) J_1(\mu_m b)}{\varepsilon_0 \mu_m^3 a^2 [J_1(\mu_m a)]^2} \left[1 - e^{-\frac{\mu_m L}{2}} \cosh(\mu_m z)\right]$.

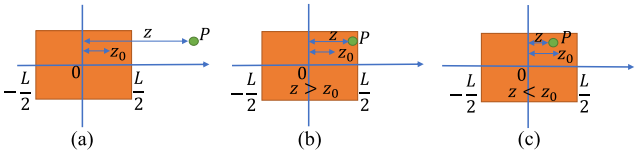

FIG. 10. Space charge potential for (a) outside when $z > z_0$, (b) inside when $z > z_0$, and (c) inside when $z < z_0$, for positive z.

In summary, the space charge potential outside and inside of the cylindrical disk charge of radius b located from $z = -L/2$ to $L/2$ inside an earthed conducting cylinder of radius a is, respectively,

$$V_1 = \frac{2ab\rho_c}{\varepsilon_0}\sum_{m=1}^{\infty}\frac{J_1(\mu_m b)J_0(\mu_m r)}{(\mu_m a)^3[J_1(\mu_m a)]^2}e^{-\mu_m|z|}\sinh\left(\frac{\mu_m L}{2}\right) \quad \text{(C9)}$$

for $|z| > \frac{L}{2}$ and

$$V_2 = \frac{2ab\rho_c}{\varepsilon_0}\sum_{m=1}^{\infty}\frac{J_1(\mu_m b)J_0(\mu_m r)}{(\mu_m a)^3[J_1(\mu_m a)]^2}\left[1 - e^{-\frac{\mu_m L}{2}}\cosh(\mu_m z)\right] \quad \text{(C10)}$$

for $|z| \le \frac{L}{2}$.

By integrating Eqs. (C9) and (C10) over r from 0 to b and taking average over the disk surface, we get

$$V_{avg1} = \frac{\int_0^b 2\pi r V_1 dr}{\pi b^2} = \frac{4a^2\rho_c}{\varepsilon_0}\sum_{m=1}^{\infty}\frac{1}{(\mu_m a)^4} \times\left[\frac{J_1(\mu_m b)}{J_1(\mu_m a)}\right]^2 e^{-\mu_m|z|}\sinh\left(\frac{\mu_m L}{2}\right) \quad \text{(C11)}$$

for $|z| > \frac{L}{2}$ and

$$V_{avg2} = \frac{\int_0^b 2\pi r V_2 dr}{\pi b^2} = \frac{4a^2\rho_c}{\varepsilon_0}\sum_{m=1}^{\infty}\frac{1}{(\mu_m a)^4} \times\left[\frac{J_1(\mu_m b)}{J_1(\mu_m a)}\right]^2\left[1 - e^{-\frac{\mu_m L}{2}}\cosh(\mu_m z)\right] \quad \text{(C12)}$$

for $|z| \le \frac{L}{2}$.

Then, we differentiate Eqs. (C11) and (C12) in terms of z to get the electric field, $E_{sc} = -\frac{dV_{avg}}{dz}$, which reads

$$E_{sc1} = \mathrm{sgn}(z)\frac{4\rho_c}{\varepsilon_0}\sum_{m=1}^{\infty}\frac{1}{\mu_m}\frac{[J_1(\mu_m b)]^2}{(\mu_m a)^2[J_1(\mu_m a)]^2}e^{-\mu_m|z|}\sinh\left(\frac{\mu_m L}{2}\right) \quad \text{(C13)}$$

for $|z| > L/2$ and

$$E_{sc2} = \frac{4\rho_c}{\varepsilon_0}\sum_{m=1}^{\infty}\frac{1}{\mu_m}\frac{[J_1(\mu_m b)]^2}{(\mu_m a)^2[J_1(\mu_m a)]^2}e^{-\frac{\mu_m L}{2}}\sinh(\mu_m z) \quad \text{(C14)}$$

for $|z| \le L/2$.

APPENDIX D: EQUATION OF MOTION AND KINETIC ENERGY

The equation of motion is $m\frac{d}{dt}u_s = eE$. If the force acts at right angles to the direction of motion, then transverse mass, $\frac{m_0}{\sqrt{1-\frac{u_0^2}{c^2}}}$, is used, but if the force acts in the direction of the motion of the electrons, then longitudinal mass, $\mathrm{m} = \frac{m_0}{\left(1-\frac{u_0^2}{c^2}\right)^{3/2}}$, is used.[18] Therefore, in our case,

$$\frac{d}{dt}u_s = \frac{e}{m_0}\left(1 - \frac{u_0^2}{c^2}\right)^{3/2}E. \quad \text{(D1)}$$

In the presence of space charge, the equation of motion for the ith disk is,[18,26]

$$\frac{du_{s_i}}{dt} = \eta\left(1 - \frac{u_0^2}{c^2}\right)^{3/2}\left[E_z(z_i)\cos(\omega t) + \sum_{j=1}^{N_D} SC\frac{Q}{e}E_{sc1,2}(z_i - z_j)\right]. \quad \text{(D2)}$$

Here, the number of electrons in one disk is $\frac{Q}{e}$, where Q is the charge in the disk, $Q = \frac{I_b}{fN_D}$,[26] f is the frequency, $E_z(z)$ is the field due to the gap given in Eq. (B4), and E_{sc1} and E_{sc2} are given by Eqs. (C13) and (C14) with the shift of the center of the jth disk to z_j, respectively, with setting $\rho_c = \frac{q}{\pi b^2 L} = \frac{e}{\pi b^2 L}$.

The kinetic energy of a relativistic electron is $KE = mc^2 - m_0c^2$, where the relativistic mass is $m = m_0/\sqrt{1-\frac{u_s^2}{c^2}}$ and the charge to mass ratio is $\eta = \frac{e}{m_0}$. Therefore, $KE = m_0c^2\left(1/\sqrt{1-\frac{u_s^2}{c^2}} - 1\right) = \frac{e}{\eta}c^2\left(1/\sqrt{1-\frac{u_s^2}{c^2}} - 1\right)$. Accordingly, the kinetic energy of the charge disks at the kth time step is calculated by

$$KE_k = \frac{Q}{\eta}c^2\sum_{j=1}^{N_D}\left(1/\sqrt{1-\frac{u_{s_{k,j}}^2}{c^2}} - 1\right). \quad \text{(D3)}$$

REFERENCES

[1] J. Benford, E. Schamiloglu, J. Stephens, J. A. Swegle, and P. Zhang, *High Power Microwaves*, 4th ed. (CRC Press, Abingdon, Oxon, Boca Raton, FL, 2025).
[2] K. L. Jensen, *Introduction to the Physics of Electron Emission*, 1st ed. (John Wiley & Sons, Inc., Hoboken, NJ, 2017).
[3] V. E. Rodyakin, V. M. Pikunov, and V. N. Aksenov, "A high power W-band extended interaction klystron with a hollow electron beam," Moscow Univ. Phys. Bull. **76**(2), 89–96 (2021).
[4] C. M. Armstrong, E. C. Snively, M. Shumail, C. Nantista, Z. Li, S. Tantawi, B. W. Loo, R. J. Temkin, R. G. Griffin, J. Feng, R. Dionisio, F. Mentgen, N. Ayllon, M. A. Henderson, and T. P. Goodman, "Frontiers in the application of RF vacuum electronics," IEEE Trans. Electron Devices **70**, 2643–2655 (2023).
[5] P. Zhang, L. K. Ang, and A. Gover, "Enhancement of coherent Smith-Purcell radiation at terahertz frequency by optimized grating, prebunched beams, and open cavity," Phys. Rev. Spec. Top.-Accel. Beams **18**(2), 020702 (2015).
[6] P. Wong, P. Zhang, and J. Luginsland, "Recent theory of traveling-wave tubes: A tutorial-review," Plasma Res. Express **2**(2), 023001 (2020).
[7] P. Zhang, B. Hoff, Y. Y. Lau, D. M. French, and J. W. Luginsland, "Excitation of a slow wave structure," Phys. Plasmas **19**(12), 123104 (2012).
[8] C. F. Dong, P. Zhang, D. Chernin, Y. Y. Lau, B. W. Hoff, D. H. Simon, P. Wong, G. B. Greening, and R. M. Gilgenbach, "Harmonic content in the beam current in a traveling-wave tube," IEEE Trans. Electron Devices **62**(12), 4285–4292 (2015).
[9] M. Arifuzzaman Faisal and P. Zhang, "Grating optimization for Smith–Purcell radiation: Direct correlation between spatial growth rate and starting current," IEEE Trans. Electron Devices **70**(6), 2860–2863 (2023).
[10] V. Y. Rodyakin, V. M. Pikunov, and V. N. Aksenov, "Current limitations for the axially symmetric hollow electron beam in the drift tubes of millimeter-wave vacuum electronic devices," Moscow Univ. Phys. Bull. **74**(6), 614–619 (2019).
[11] A. V. Haeff and L. S. Nergaard, "A wide-band inductive-output amplifier," Proc. IRE **28**(3), 126–130 (1940).
[12] R. Heppinstall and G. T. Clayworth, "The inductive output tube: The latest generation of amplifier for digital terrestrial television transmission," EBU Tech. Rev. Autumn, 1997.
[13] A. V. Haeff, "Electron discharge device," U.S. Patent 2,237,878, 1941.

[14]D. R. Whaley, B. M. Gannon, V. O. Heinen, K. E. Kreischer, C. E. Holland, and C. A. Spindt, "Experimental demonstration of an emission-gated traveling-wave tube amplifier," IEEE Trans. Plasma Sci. **30**(3), 998–1008 (2002).
[15]L. Jin, Y. Zhou, and P. Zhang, "Direct density modulation of photo-assisted field emission from an RF cold cathode," J. Appl. Phys. **134**(7), 074904 (2023).
[16]H. P. Freund, T. Bui, R. L. Ives, T. Habermann, and M. Read, "Comprehensive design and whole-cavity simulation of a multi-beam inductive output tube using a 3rd harmonic drive on the grid," IEEE Trans. Plasma Sci. **52**, 727–737 (2024).
[17]H. P. Freund, R. L. Ives, and W. Sessions, "High-efficiency inductive output tubes using a 3rd harmonic drive on the grid," IEEE Trans. Plasma Sci. **48**, 3827–3831 (2020).
[18]R. G. Carter, *Microwave and RF Vacuum Electronic Power Sources*, 1st ed. (Cambridge University Press, 2018).
[19]R. G. Carter, "Simple model of an inductive output tube," in *2009 IEEE Int. Vac. Electron. Conf.* (IEEE, Rome, Italy, 2009), pp. 427–428.
[20]R. G. Carter, "Simple model of an inductive output tube," IEEE Trans. Electron Devices **57**(3), 720–725 (2010).
[21]J. E. Rowe, H. G. Booker, and N. Declaris, *Nonlinear Electron-Wave Interaction Phenomena* (Elsevier Science, Saint Louis, 2013).
[22]J. R. Hechtel, "The effect of potential beam energy on the performance of linear beam devices," IEEE Trans. Electron Devices **17**(11), 999–1009 (1970).
[23]J. R. M. Vaughan, "Calculation of coupled-cavity TWT performance," IEEE Trans. Electron Devices **22**(10), 880–890 (1975).
[24]Y. Chen, S. Fu, Z. Huang, and Z. Zhang, "Nonlinear space charge effect of Gaussian type bunched beam in Linac," in *Proceedings of the Part. Accel. Conf.* (IEEE, Dallas, TX, 1995), pp. 3343–3345.
[25]Y. Chen, "Space charge effect of bunched beam with different distributions in Linac," *3rd European Particle Accelerator Conference (EPAC1992)*, p 765 (1992).
[26]R. Carter and J. Feng, "The design of high power, high efficiency, multi-beam klystrons," *The Compact Linear Collider (CLIC) meeting 2003*, 09-May-2003, CERN (2003).
[27]J. R. Hechtel, "DC-to-RF energy conversion in ungridded klystron gaps," IEEE Trans. Electron Devices **16**(2), 212–217 (1969).
[28]A. Iqbal, D. Wen, J. Verboncoeur, and P. Zhang, "Recent advances in multipactor physics and mitigation," High Voltage **8**(6), 1095–1114 (2023).
[29]R. Lawrence Ives and R. J. Michael Read, "Development of a 402.5 MHz 140 kW inductive output tube," Final Report, 1039691, 2012.
[30]W. E. Waters, "Space-charge effects in klystrons," IRE Trans. Electron Devices **4**(1), 49–58 (1957).
[31]J. F. Orrett, A. J. Moss, P. Corlett, and S. Buckley, "IOT testing at the ERLP," in *Proceedings of EPAC 2006*, June 26-30, 2006, Edinburgh, Scotland 1382–1384 (2006).
[32]J. P. Verboncoeur, A. B. Langdon, and N. T. Gladd, "An object-oriented electromagnetic PIC code," Comput. Phys. Commun. **87**(1–2), 199–211 (1995).
[33]Y. Y. Lau, M. Friedman, J. Krall, and V. Serlin, "Relativistic Klystron amplifiers driven by modulated intense relativistic electron beams," IEEE Trans. Plasma Sci. **18**(3), 553–569 (1990).
[34]C. B. Wilsen, J. W. Luginsland, Y. Y. Lau, T. M. Antonsen, D. P. Chernin, P. M. Tchou, M. W. Keyser, M. Keyser, R. Gilgenbach, and L. Ludeking, "A simulation study of beam loading on a cavity," IEEE Trans. Plasma Sci. **30**(3), 1160–1168 (2002).
[35]R. Kowalczyk, Y. Y. Lau, T. M. Antonsen, J. W. Luginsland, D. P. Chernin, C. B. Wilsen, W. Tang, and R. M. Gilgenbach, "AC space charge effects on beam loading of a cavity," IEEE Trans. Electron Devices **52**(9), 2087–2095 (2005).
[36]G. Caryotakis, "Klystrons," in *Modern Microwave and Millimeter-Wave Power Electronics*, edited by R. J. Barker, N. C. Luhmann, J. H. Booske, G. S. Nusinovich (IEEE Press: Wiley-Interscience, Hoboken, NJ, 2005).
[37]W. R. Smythe, in *Static and Dynamic Electricity*, 3rd ed. (Hemisphere [u.a.], New York, 1989) rev. print.